INORGANIC CHEMISTRY
FRONTIERS

REVIEW

View Article Online
View Journal | View Issue

Check for updates

Cite this: *Inorg. Chem. Front.*, 2020, **7**, 2248

Intermetallic borides: structures, synthesis and applications in electrocatalysis

Hui Chen and Xiaoxin Zou *

Received 4th February 2020,
Accepted 2nd April 2020

DOI: 10.1039/d0qi00146e

rsc.li/frontiers-inorganic

Structurally ordered intermetallic borides are a large family of inorganic solids with rich bonding schemes, and huge compositional and structural diversity. The family members possess high flexibility to modulate the local electronic structures and surface adsorption properties, providing great opportunities for the development of advanced catalysts with superior activity and stability. In this review, we summarize the structural features of intermetallic borides, with emphasis on the covalent linkage patterns of boron atoms in them, and the research methods for understanding their electronic structures. We also present the recent developments in the synthesis of phase-pure, well-defined intermetallic borides, most of which are suitable for catalytic studies. We further highlight the theoretical and experimental advances in the emerging boride-catalyzed reactions and the important roles of boron in tuning electrocatalytic performances. Finally, we propose the remaining challenges and future developments of boride synthesis and catalytic applications.

1. Introduction

Intermetallic compounds with a combination of two or more metals/metalloids are a large family of inorganic solids with an ordered crystal structure and precise stoichiometry.[1] They usually have drastically different crystal and electronic structures from their corresponding constituent elements, endowing these types of compounds with some interesting properties and functionalities. Intermetallic borides represent an exotic class of inorganic compounds with high compositional richness and structural diversity.[2] Boron is found to alloy with almost all metals in the periodic table to form intermetallic borides. The earliest report of borides dates back to the early 19th century, and several metals (*e.g.*, Pt, Fe, Al and Mg) were known to be able to combine with boron at the end of 19th century.[3–5] In the 1930s to 1970s, a great number of intermetallic borides, covering the majority of alkali, alkaline-earth, transition metal and lanthanide metal elements, were explored at

State Key Laboratory of Inorganic Synthesis and Preparative Chemistry, College of Chemistry, Jilin University, 2699 Qianjin Street, Changchun 130012, China. E-mail: xxzou@jlu.edu.cn

Hui Chen

Hui Chen received his PhD in materials science from Jilin University in 06/2018. He is currently a postdoctoral researcher at the State Key Laboratory of Inorganic Synthesis and Preparative Chemistry in Jilin University. His research interests focus on the synthesis and applications of functional inorganic materials in chemical sensing and catalysis.

Xiaoxin Zou

Xiaoxin Zou was awarded a PhD in Inorganic Chemistry from Jilin University (China) in 06/2011; and he then moved to the University of California, Riverside and Rutgers, The State University of New Jersey, as a postdoctoral scholar from 07/2011 to 10/2013. He is currently a professor at the State Key Laboratory of Inorganic Synthesis and Preparative Chemistry in Jilin University. His research interests include electrocatalysis, nanocatalysis, hydrogen energy, solid state chemistry, structural chemistry, perovskites and intermetallic borides.

the crystal structure level.[6–9] At present, there are more than 200 binary and 800 ternary metal borides, which crystallize in more than 150 different structure types.[10,11] Numerous quaternary borides or larger systems are also known.[12,13]

The unusual intrinsic chemical nature of boron endows intermetallic borides with an extremely large variety of structures. Compared with other non-metal atoms (*e.g.*, O, S, N) in the corresponding metal compounds such as oxides, sulfides and nitrides, the boron atom in borides has some notable features (Fig. 1). Boron is a metalloid element with an intermediate electronegativity value (2.04 in the Pauling scale) between metals (M) and non-metals. When alloyed into intermetallic borides, constituent elements can generate rich bonding schemes in one compound, including metallic M–M/M–B bonds, ionic M–B bonds and covalent B–B bonds. The other inherent property of boron is that boron has less valence electrons than valence orbitals. This electron-deficient characteristic allows boron atoms to present abundant types of covalent linkage patterns in different boride lattices.[14] Such an amazing variety of chemical bondings in borides does not exist in other inorganic material systems such as sulfides, oxides and nitrides, in which non-metal atoms (*i.e.*, O, S, N) mainly bond with metal atoms.

The compositional and structural richness of intermetallic borides, together with the inherent chemical nature of boron, offers great opportunities to encourage many novel discoveries. Early in the 1950s, the superconducting properties of borides were investigated.[15,16] MgB_2, a newly discovered superconductor, is known to have the highest transition temperature (T_c = 39 K) among intermetallic superconductors.[17] Another remarkable property of borides is high hardness. In 2005, Kaner *et al.* predicted that superhard materials may be created by combining boron with some transition metals (*e.g.*, Re, Os, and Ir).[18] Chung *et al.* then synthesized ReB_2 and confirmed its superhard nature.[19] The discovery of ReB_2 ignited extensive works focusing on the hardness of borides, and some boron-rich borides (*e.g.*, FeB_4 and WB_4) are reported as promising superhard materials.[20–22] Besides, many borides have exhibited other impressive properties in bulk, including permanent magnetism in $Nd_2Fe_{14}B$,[23,24] the magnetocaloric effect in $AlFe_2B_2$,[25] thermoelectric properties in CaB_6 and YB_{66},[26–28] lithiophilicity for lithium metal batteries in LiB,[29] and as a sulfur host for lithium–sulfur batteries.[30–32] These versatile functions of intermetallic borides beyond the corresponding metals demonstrate the essential role of boron in the modulation of bulk properties.

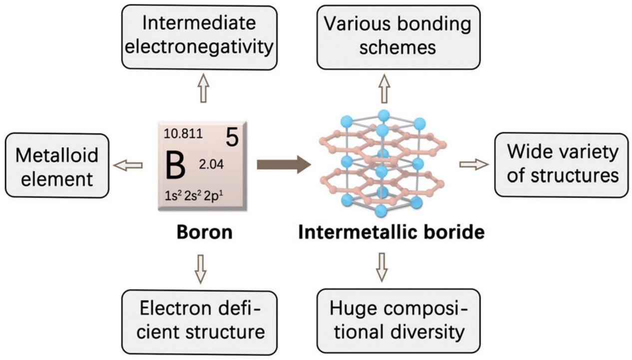

Fig. 1 A schematic summary of the structural features of boron and intermetallic boride.

In addition to bulk properties, borides have attracted great interest due to their surface catalytic properties. The catalytic application of borides started to develop since the 1950s. In the pioneering work of Paul *et al.*, nickel boride (Ni_2B) containing small quantities of active promoters (*e.g.*, Mo, W, Cr) were discovered to be more active for the hydrogenation reaction than RANEY® nickel.[33] Many boride catalysts have already been found to be active in various chemical reactions, such as hydrogenation of different organic compounds,[34,35] hydrotreating,[36] and hydrogen generation from borohydride hydrolysis.[37] However, a vast majority of the reported boride catalysts refer to amorphous boride phases, often prepared by a widely adopted borohydride reduction method in solution at low temperature. Their exact composition and catalytically active species have largely remained in the dark.

It is only in the last decade that the huge potential of boride catalysts with a well-defined structure was revealed, accompanied by the increased focus on energy-related electrocatalysis. Particularly the past five years have seen a surge of intense research on boride catalysts. Large amounts of well-known transition metal borides gain renewed attention, and many of them are identified as highly active and stable electrocatalysts for the hydrogen evolution reaction (HER) or oxygen evolution reaction (OER). Demands for effective electrocatalytic properties also greatly stimulate the recent development of preparation methods for the selective and general synthesis of borides that have different composition, stoichiometry and variable crystal phases. Furthermore, the rapid process of computational chemistry promotes the understanding of the roles of boron atoms in the modulation of electronic structure, surface adsorption and catalytic abilities.

In this review, we focus on the recent advances of well-defined boride catalysts. We start by giving an introduction of crystal structure, electronic structure and bonding characteristics in metal borides. We then describe some newly reported synthesis of borides, with discussion on their advantages and limitations. After that, we examine the emerging electrocatalytic applications of crystalline borides, paying particular attention to the hydrogen evolution reaction. Finally, we provide our perspectives on the challenge and several future directions of boride catalysts.

2. Crystal and electronic structures

The subsequent sections mainly discuss binary metal borides, since the number of structure types of known metal borides is too great to present them in their entirety. Here we note that the definition of "boride" refers to the ordered intermetallic boride with a well-defined structure, and does not include

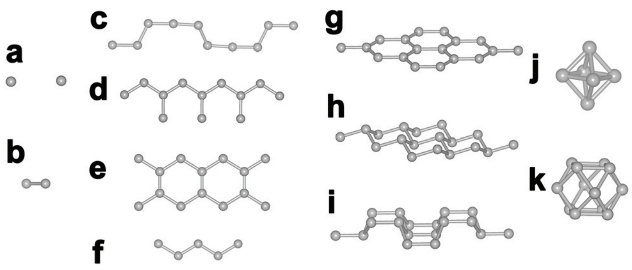

Fig. 2 Possible types of covalent linkage patterns of boron atoms in different crystal lattices. (a) Isolated boron atoms (*e.g.*, Ni_3B); (b) paired boron atoms (*e.g.*, V_3B_2); (c) puckered boron chains (*e.g.*, Ni_4B_3); (d) branched boron chains (*e.g.*, $Ru_{11}B_8$); (e) double boron chains (*e.g.*, V_3B_4); (f) zig-zag boron chains (*e.g.*, NiB); (g) graphene-like flat boron layers (*e.g.*, TiB_2); (h) puckered boron layers with "chair" configuration (*e.g.*, ReB_2); (i) puckered boron layers with "boat" configuration (*e.g.*, RuB_2); (j) B_6 octahedron (*e.g.*, YB_6); (k) B_{12} cuboctahedra (*e.g.*, YB_{12}).

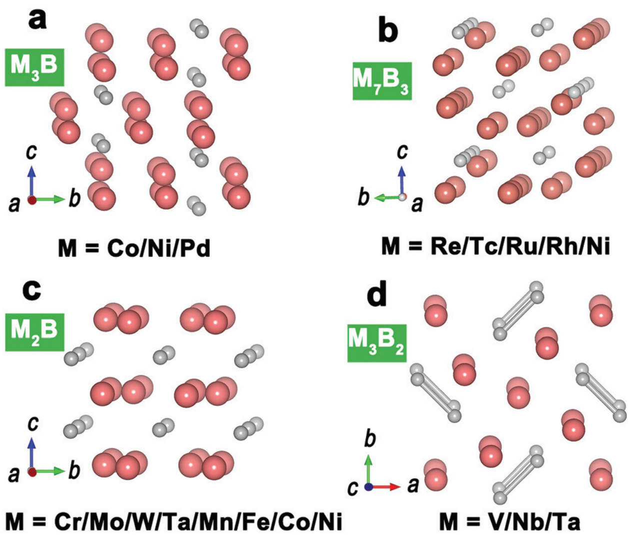

Fig. 3 Representative crystal structures of (a) M_3B; (b) M_7B_3; (c) M_2B; (d) M_3B_2. Metal atoms and boron atoms are in pink and grey, respectively.

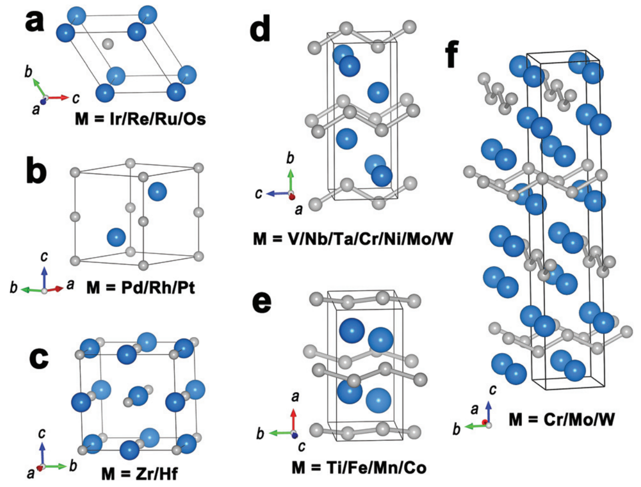

Fig. 4 Crystal structures of (a) WC-type monoboride; (b) anti-NiAs-type monoboride; (c) NaCl-type monoboride; (d) CrB-type monoboride; (e) TiB-type monoboride; (f) MoB-type monoboride. Metal atoms and boron atoms are in blue and grey, respectively.

amorphous (or disordered) borides and boron-doped materials. According to the data from the Inorganic Crystal Structure Database (ICSD), intermetallic borides of transition metals take the highest proportion (about 55%) in the family of binary borides, followed by intermetallic borides of lanthanides (about 25%). The vast majority of metal borides (more than 80%) have a metal to boron ratio ranging from 3 : 1 (M_3B) to 1 : 12 (MB_{12}), with the exception of few borides of alkali-earth metals and lanthanides (*e.g.*, Be_4B, Mg_2B_{25}, YB_{66}). With the increase of boron content, the covalent linkage patterns of boron atoms in borides evolve from isolated boron to one-dimensional boron chains, two-dimensional (2D) boron layers and three-dimensional (3D) boron frameworks composed of boron clusters (Fig. 2). The arrangement of boron atoms in the crystal structure plays an important role in determining the physical and chemical properties of borides.

2.1. Metal-rich borides

For metal-rich borides (M_xB, $x > 1$), M_3B, M_7B_3, M_2B and M_3B_2 are four representative structural types (Fig. 3), in which the component M refers to some transition metals (*e.g.*, Ni, Co). Their metal atoms are connected together with metallic bonds to generate a 3D metal skeleton. Boron atoms/pairs are dispersed in the metal skeleton with M–B bonds. In the structures of M_3B, M_7B_3 and M_2B (Fig. 3a–c), boron atoms are isolated because the neighboring B–B distance is too long to generate B–B bonds. As for M_3B_2 (Fig. 3d), boron atoms are paired off in a short B–B distance (0.18–0.19 nm), which is near to the B–B distance in elemental boron (about 0.175 nm).

2.2. Monoborides

Boron can be alloyed with many transition metals to form intermetallic monoborides (MB). Depending on metal species, the monoborides can be classified into different structural types (Fig. 4), containing WC-type, anti-NiAs-type, NaCl-type, CrB-type, TiB-type and MoB-type. Metal atoms in these monoborides hold similar packing arrangements to the parent metals, while the incorporation of interstitial boron atoms results in the expansion of crystal lattices to a certain extent. Isolated boron atoms are observed in the structures of WC-type, anti-NiAs-type and NaCl-type monoborides (Fig. 4a–c). As for CrB-type and TiB-type monoborides (Fig. 4d and e), boron atoms form zig-zag chains parallel to the *c*-axis and *b*-axis, respectively. MoB-type monoborides (Fig. 4f) possess zig-zag boron chains in two mutually perpendicular directions.

2.3. Diborides

Metal diborides (MB_2) are a large family consisting of at least 30 members, covering many transition metals, lanthanides and main group elements. These diborides belong to three structure types (Fig. 5), containing twenty eight AlB_2-type diborides, two ReB_2-type diborides and two RuB_2-type dibor-

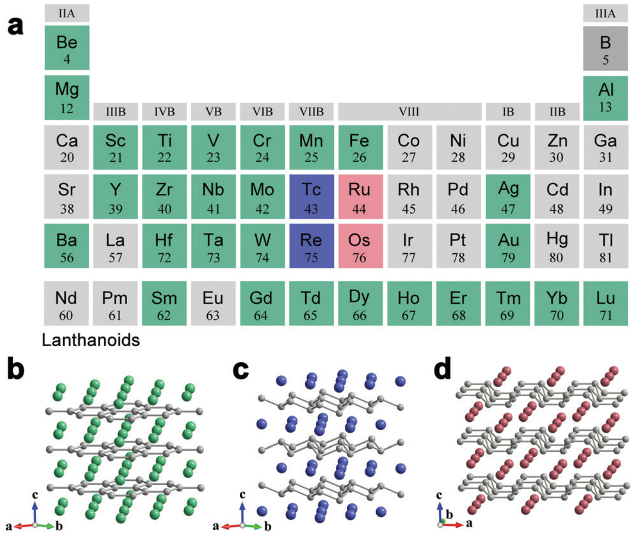

Fig. 5 (a) Elements constructing metal diborides. Crystal structures of (b) AlB_2-type diboride; (c) ReB_2-type diboride; (d) RuB_2-type diboride. Boron is in grey, and metals used for constructing the AlB_2-type, ReB_2-type and RuB_2-type diborides are in green, blue and pink, respectively. Reproduced with permission from ref. 38. Copyright 2019 Wiley-VCH.

ides.[38] They comprise 3D metallic frameworks and 2D boron layers as subunits, endowing diborides with high electrical conductivity. Boron layers in AlB_2-type diborides are graphene-like borophene structures (Fig. 5b), while in ReB_2-type and RuB_2-type diborides are puckered layers with "chair" configuration (Fig. 5c) and "boat" configuration (Fig. 5d), respectively.

2.4. Boron-rich borides

In boron-rich systems (MB_x, $x > 2$), the boron atoms are often bonded covalently to form boron cages/clusters as structural units which are further linked together to generate a 3D boron skeleton. For CrB_4, FeB_4 (Fig. 6a), and MnB_4 (with a similar structure to CrB_4), B–B bonds form boron cages as the structural unit, while for MB_4 with M = lanthanide (Ln) and actinide (An) series, the structural units are B_6 octahedra linked by B–B pairs (Fig. 6b). The other two dominant structural types in boron-rich borides are MB_6 and MB_{12}, which mainly occur in lanthanides–boron and actinides–boron systems. The structures of MB_6 (Fig. 6c) and MB_{12} (Fig. 6d) are composed of a 3D boron network based on B_6 octahedra and B_{12} cuboctahedra, respectively. Some rare-earth and alkaline-earth metals can even form borides with a B/M ratio above 12 (*e.g.*, Na_2B_{29}, YB_{66}), in which the basic structural unit is a 3D boron framework consisting of B_{12} icosahedra.[39,40] In these boron-rich borides, the metal atoms are embedded in the pores of the boron skeleton, and provide the electron-deficient boron cages/clusters with external bonding electrons.

2.5. Electronic and bonding properties

The electronic structure and bonding characteristics of metal borides strongly depend on the constituent metal, stoichiometry and crystal structure. Density functional theory (DFT) calculations have been powerful tools to analyze the electronic and bonding properties of borides. The density of states (DOS) and projected DOS can be employed to understand some electronic properties, including electrical conductivity, metal d-band properties, and orbital hybridization. The crystal orbital overlap population (COOP), the crystal orbital Hamiltonian population (COHP), and the electron localized function (ELF) method are available for obtaining information on chemical bonding. Bader charge analysis can be used to evaluate charge transfer.

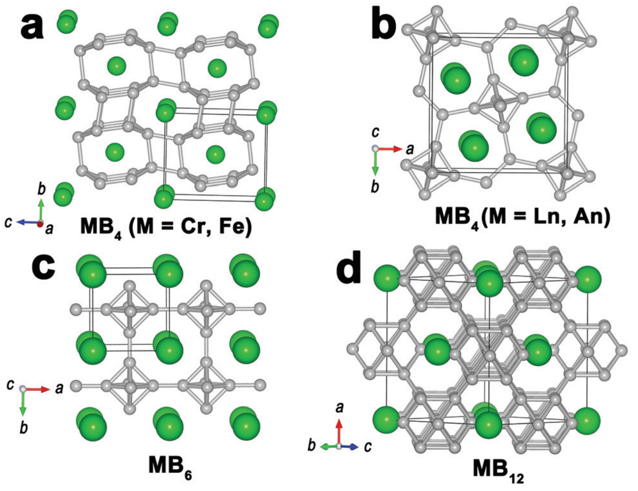

Fig. 6 Crystal structures of (a) MB_4 (M = Cr, Fe); (b) MB_4 (M = Y, La, Ce, Pr, Nd, Sm, Gd, Tb, Dy, Ho, Er, Tm, Yb, Lu, Th, U and Pu); (c) MB_6 (M = K, Ca, Sr, Ba, Y, La, Ce, Pr, Nd, Sm, Eu, Gd, Tb, Dy, Ho, Er and Tm); (d) MB_{12} (M = Zr, Hf, Y, Gd, Tb, Dy, Ho, Er, Tm, Yb, Lu, Th, U and Pu). Metal atoms and boron atoms are in green and grey, respectively.

Taking as an example RuB, its Fermi level is crossed by the DOS (Fig. 7a), indicating metallic properties.[41] The Ru d-band contributes to the majority of the total d states of RuB, and the Ru d-band filling in RuB shows minor changes compared to the corresponding pure Ru metal. The pDOS and COHP demonstrate a strong orbital hybridization between Ru 4d states and B 2sp states in RuB (Fig. 7a and b), leading to broadening of the Ru d-band and downshift of the d-band center. In addition, the intensity of metal–boron hybridization in different intermetallic borides depends on the boron content and crystal structure. With the increase of boron content in four Ru–B intermetallics (*i.e.*, Ru_7B_3, Ru_2B_3, RuB, RuB_2), the integrated COHP values of Ru–B drop gradually, suggesting the decreased intensity of Ru–B hybridization (Fig. 7c).[42] This is because stronger B–B interactions in more boron-rich environments weaken the orbital hybridization between Ru 4d and B 2sp states.

Bader charge analysis presents a negligible charge transfer between metal and boron ($<0.15|e|$) in four Ru–B intermetallics due to the similar electronegativity of Ru and B. However, the charge transfer between metal atoms and B atoms in different metal borides is non-constant. For example, Fig. 7d shows the charge transfer from metal atoms to adjacent boron atoms on a family of metal diborides. The charge transfer

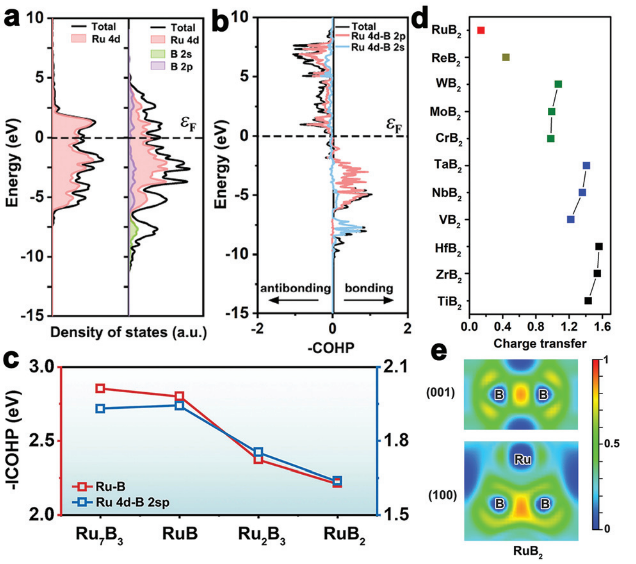

Fig. 7 (a) Calculated DOS and pDOS of the RuB (001) surface and Ru (0001) surface. (b) Integrated COHP of the Ru–B bond in RuB. Reproduced with permission from ref. 41. Copyright 2020 Wiley-VCH. (c) The integrated COHP of Ru_7B_3, Ru_2B_3, RuB and RuB_2. (d) Charge transfer from metal atoms to boron atoms on a family of metal diborides. (e) ELF of two planes for RuB_2. Reproduced with permission from ref. 42. Copyright 2020 Royal Society of Chemistry.

value generally decreases in the order: Group VIII-diborides (*i.e.*, RuB_2) < Group VII B-diborides (*i.e.*, ReB_2) < Group VI B-diborides (*i.e.*, CrB_2, MoB_2, WB_2) < Group V B-diborides (*i.e.*, VB_2, NbB_2, TaB_2) < Group IV B-diborides (*i.e.*, TiB_2, ZrB_2, HfB_2). The tiny amount of charge transfer between Ru and B, combined with the ELF analysis in Fig. 7e, demonstrate that the Ru–B interaction in RuB_2 is metallic.[42]

The electronic structure plays a fundamental role in determining the surface adsorption energy and catalytic properties of borides toward various reactions. Several recent studies have found that the HER activities of borides are strongly related to metal d-band properties (*i.e.*, d-band center, d-band width) which influence the adsorption strength of key hydrogen intermediates.[41–43] The metal d-band properties of boride catalysts depend on many factors including metal–boron orbital hybridization, metal–metal bond length and metal–boron charge transfer. For example, the position of the metal d-band center in RuB_2 is close to that of the benchmark Pt catalyst, leading to optimal hydrogen adsorption and Pt-like activity for the HER.[43] When employed as OER catalysts, borides often undergo surface reconstruction to form boron-containing amorphous oxide layers,[44,45] in which the catalytically active phase remains poorly understood. Thus, the essential connection between the electronic structure of borides and OER performance is currently not well established. In addition, research into borides as nitrogen reduction reaction (NRR) catalysts remains at an early stage. Recent theoretical work revealed that boron p_z-orbital filling is an important parameter to control the activation of N_2.[46] Further electronic structure studies on boride catalysts for the NRR are urgently desired.

3. Synthetic methods

The difficulty of obtaining phase-pure, catalysis-applicable samples is a significant roadblock to extensively study the catalytic functions of intermetallic borides. This can be reflected by the three facts: (i) traditional solid-state methods for preparing borides with well-defined structures require high temperature and pressure conditions. The resulting samples are often made of bulk particles in a small quantity, which are suitable for their physical properties, but difficult to branch out for studying catalytic abilities. (ii) Although a few mild synthesis routes are employed to yield borides, the obtained materials are severely limited in elemental composition and crystal phase. (iii) Most metal–boron systems possess multiple phases with slight stoichiometric differences, making it difficult to accurately prepare the phase-pure target borides. In this section, we summarize the recent development of the typical synthesis of intermetallic borides. These synthesis advances usually include the following characteristics: a relatively low temperature synthetic route; general synthesis covering a range of metal elements; selective synthesis of multiple crystal phases with different stoichiometries.

3.1. Element reaction route

The element reaction route is a common method for boride synthesis. In this synthetic scheme, borides are typically obtained by sintering of elemental metal and boron mixture under vacuum or inert gas. The sintering procedure is often performed under extreme conditions in a high pressure–high temperature apparatus (Fig. 8a) or arc-melting chamber.[47] For example, Chen *et al.* recently synthesized several Mo–B phases with different crystal phases including Mo_2B, MoB, α-MoB_2 and β-MoB_2 at a high pressure of 5.2 GPa and a high tempera-

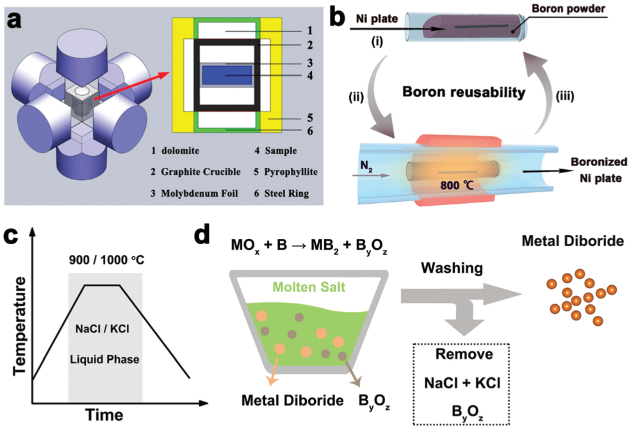

Fig. 8 (a) Schematic of a high pressure–high temperature apparatus. Reproduced with permission from ref. 47. Copyright 2018 the American Chemical Society. (b) Schematic of the boron reuse synthesis of boronized Ni sheets. Reproduced with permission from ref. 45. Copyright 2019 Royal Society of Chemistry. (c) The reaction temperature between MO_x and B precursors occurs in the liquid phase domain of molten salts. (d) Schematic diagram of the synthesis of metal diborides. Reproduced with permission from ref. 71. Copyright 2019 Royal Society of Chemistry.

ture of 1600–1800 °C.[48] Some borides, including WB_3,[49] MnB,[50] Mn_3B_4,[51] and MoB_4,[52] were also synthesized successively with a high pressure and high temperature method. In addition, Fokwa's group employed the arc-melting procedures to prepare several Mo–B phases (*i.e.*, Mo_2B, α-MoB, β-MoB, and α-MoB_2), containing about 10% weight percentage of impurity phases.[53] Subsequently, this group further improved the synthesis method by performing in a Sn flux to promote the reactivity and diffusion of solid reactants, obtaining single-phase Mo_2B_4 samples.[54] The metal flux methods have also been utilized to obtain single crystals of intermetallic borides (*e.g.*, MgB_2, CaB_6).[55,56] It should be noted that excess boron is often necessary for preparing many boride phases during the element reaction, leading to inevitable boron contamination in the resulting samples to some extent.

The direct reaction between metal sheets and boron powders can be used for the preparation of boronized metal sheets. Our group explored the strategy for generally transforming a variety of metal sheets (*e.g.*, Fe, Co, Ni, NiFe alloy and SUS 304 stainless steel) into boronized metal sheets as self-supported OER electrodes.[44] The boronization technique using boron and potassium fluoroborate as the boronizing agent was capable of generating single-phase M_2B layers on the base metal sheets. Later, our group realized the feasible growth of Ni_3B layers on nickel sheets by improving the boronization process.[45] The excess boron powder was found can be reusable in the cyclic synthesis procedure for obtaining boronized Ni plates (Fig. 8b).

3.2. Thermal reduction route

The method contains many chemical reaction types, often using metal oxides, halides or sulfides as metal sources. Thanks to the various reducing agents available in the method, many typical reactions, including the solid-state metathesis reaction and metallothermic reduction reaction, were developed to realize simple, rapid or general synthesis of borides.

3.2.1. Boron source as the reducing agent. The main reducing agents comprising boron are elemental boron, boranes, borohydrides and alkaline-earth borides. These reducing agents work at different reaction systems, thus producing borides with different crystallinities and morphologies. For instance, some boranes (*e.g.*, B_2H_6, B_5H_9) as volatile precursors were applied in the chemical vapor deposition (CVD) synthesis of boride nanowires,[57–59] while borohydrides (*e.g.*, KBH_4, $NaBH_4$) were widely involved in solution synthesis routes to obtain amorphous (or low crystalline) boride nanostructures.[60–67] Elemental boron or alkaline-earth borides (*e.g.*, MgB_2) were available for solid phase reduction of metal sources, accompanied by the generation of boride particles.[68–70] Very recently, our group employed the boron thermal reaction between boron powder and metal oxide under KCl–NaCl molten salt conditions to prepare phase-pure borides (Fig. 8c and d).[71] The molten salt-assisted routes could generally produce a family of MB_2 (M = Ti, V, Cr, Mn, Zr, Nb, Mo, Hf, Ta, W, Re and Ru) at a relatively low temperature of 900–1000 °C. In another significant work, Okada *et al.* successfully prepared $LEAlB_{14}$ (LE = Li, Mg) compounds by using boron powders and various metal salts as starting materials in a high temperature Al flux.[72]

The solid-state metathesis reaction between metal halides and alkaline-earth borides was another approach to dramatically lower the temperature needed for the synthesis of transition metal borides. Using the reaction between MgB_2 and anhydrous metal chloride (MCl_x), our group prepared a class of twelve MB_2 nanomaterials, covering many transition metals from Group IV B to Group VIII elements.[38] The reactions were very exothermic due to the formation of a thermodynamically stable by-product (*i.e.*, $MgCl_2$), thus requiring a relatively low heating temperature of 850–950 °C, with the exception of OsB_2 synthesized at 1100 °C.

3.2.2. Introduction of an extra reducing agent. The addition of an extra reducing agent (*e.g.*, carbon, hydrogen or metal) is necessary for some boride syntheses. Carbothermal reduction is one of the oldest methods for obtaining borides. However, this method often suffers from some contamination of carbon, boron or boron carbide in the as-prepared samples, hindering its wide use. In comparison, hydrogen can serve as both a carrier gas and reducing agent of the boron source, and thus has the advantages for creating high-quality boride layers by the CVD technique. For instance, Wang *et al.* recently fabricated ultrathin 2D Mo_3B films on Mo foils by employing hydrogen to carry the boron/boron oxide mixture as the boronizing agent (Fig. 9).[73]

The metallothermic reduction reaction between the boron source (*e.g.*, elemental boron and alkaline-earth borides), metal source (*e.g.*, metal halides and oxides) and reducing agent (*e.g.*, K, Al and Mg) is a simple and effective route to make high purity of borides at fairly low reaction temperatures. Compared with the solid-state metathesis reaction, the method possesses more flexibility to synthesize borides with different stoichiometries and crystal phases. Jothi *et al.* presented the general synthesis of metal borides using elemental boron and MCl_x with the tin (Sn) metal powder as the reducing agent.[74] The synthesis route could obtain a series of crystalline

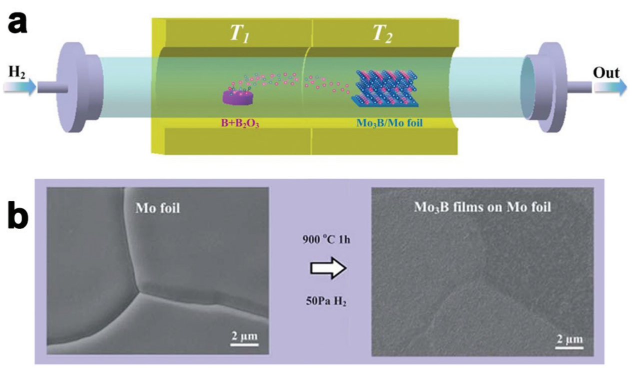

Fig. 9 (a) Schematic diagram of the growth of Mo_3B layers on Mo foils. (b) SEM images of the Mo foil before and after boronization. Reproduced with permission from ref. 73. Copyright 2017 Royal Society of Chemistry.

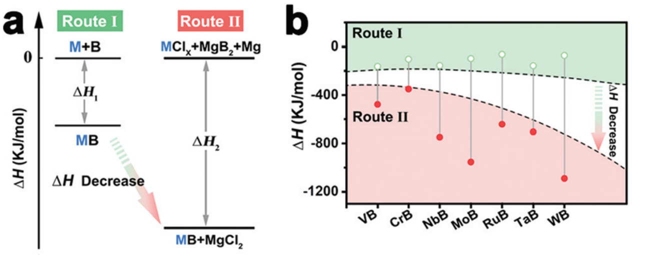

Fig. 10 (a) The comparison of the element reaction route (Route I) and magnesiothermic reduction route (Route II) for monoboride synthesis. (b) Calculated reaction enthalpies of the two reaction routes. Reproduced with permission from ref. 41. Copyright 2020, Wiley-VCH.

borides covering 3d–5d transition metals, including monoborides (*e.g.*, CoB, FeB, NbB, α-MoB and WB) and diborides (*e.g.*, VB_2, NbB_2, MoB_2, Mo_2B_4 and TaB_2). Besides being a reducing agent, the metal Sn with a low melting point (230 °C) provided a major advantage to lower the reaction temperature (between 700 °C and 900 °C). The as-prepared samples had different nanostructures, such as nanorods for MoB_2, nanosheets for CoB, nanoprisms for VB_2, nanoplates for FeB, and nanoparticles for TaB_2, NbB_2 and Mo_2B_4.

Except for metal Sn, magnesium (Mg) can also be employed as the reducing agent in boride synthesis (known as magnesiothermic reduction reaction). Very recently, our group reported the synthesis of monoborides with Mg as the reducing agent of MCl_x and MgB_2 under relatively mild conditions (Fig. 10).[41] The synthesis route produced seven phase-pure monoborides of transition metals, covering V, Nb, Ta, Cr, Mo, W and Ru. The route (*i.e.*, Route II) was more thermodynamically favorable compared with the element reaction route (*i.e.*, Route I), as demonstrated by its much more negative reaction enthalpies. The magnesiothermic reduction reaction has also been successfully extended to synthesize phase-pure intermetallic silicides (*e.g.*, RuSi and Ru_2Si_3).[75]

3.3. Precursor-directed route

The controllable synthesis of 2D boride nanosheets faces great challenges, although layered materials have demonstrated unique advantages toward catalytic applications.[76] Very recent works have successfully utilized the layered bulk materials as precursors to evolve into layered borides. The precursor refers to MAB phases, where M is a transition metal element (*e.g.*, Mo and Mn), A is a group IIIA or IVA metal element (*e.g.*, Al and In), and B is boron. MAB phases represent an emerging family of layered structural materials, mainly containing MoAlB-type (*e.g.*, WAlB and MoAlB), Cr_2AlB_2-type (*e.g.*, Mn_2AlB_2 and Cr_2AlB_2) and Cr_3AlB_4-type.[77,78] Removing the A-layer from the structure is the key to form layered boride nanomaterials because metallic M–A bonding is much weaker in strength than covalent M–B bonding. For example, Wang *et al.* reported layered TiB materials by exfoliating the In layers from Ti_2InB_2 (Fig. 11a and b).[79] The In atoms dealloy from the Ti_2InB_2 material under vacuum at high temperatures for 6 days, while the In metal possesses a low melting point and high vapor pressure. In addition, Zhang *et al.* prepared CrB nanosheets by etching Al layers out from Cr_2AlB_2 (Fig. 11c and d). The Cr_2AlB_2 powders were fully immersed in HCl solution, followed by washing and collecting the resulting suspension.[80,81] The main drawbacks of the technique lie in the difficulty of obtaining the ternary boride precursor and inefficiency of removing the A-layer from the precursor structure.

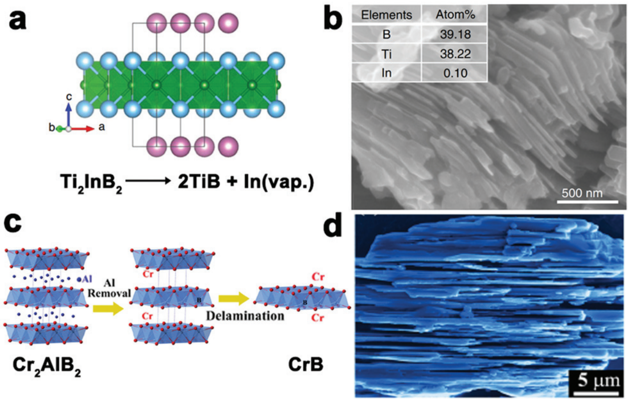

Fig. 11 (a) Crystal structures of Ti_2InB_2; (b) SEM image of the TiB phase. Reproduced with permission from ref. 79. Copyright 2019 Nature Publishing Group, 2018 Elsevier, respectively. (c) Schematic illustration of the transformation from Cr_2AlB_2 to 2D-CrB. (d) SEM images of CrB nanosheets. Reproduced with permission from ref. 80. Copyright 2018 Elsevier, respectively.

4. Catalysis applications

After carefully reviewing the progress in boride synthesis, in this section we will discuss the recent applications of intermetallic borides in electrocatalysis, including hydrogen evolution, oxygen evolution and nitrogen reduction. In addition, several comprehensive reviews concerning structurally ordered intermetallics and their versatile catalysis applications are recommended to readers for reference.[82–84]

4.1. Electrocatalytic HER

The hydrogen evolution reaction (HER) is a crucial half-reaction in many renewable energy-related fields including electrochemical water splitting, chlor-alkali processes, *etc.*[85] The HER is a two-electron transfer process with adsorbed hydrogen (H*) as a key reaction intermediate (Fig. 12a). The adsorption free energy of atomic hydrogen (ΔG_{H^*}) is a reliable descriptor to reflect the HER activity of catalysts. Platinum (Pt)-based materials are demonstrated to be the best-performing HER electrocatalysts with moderate hydrogen adsorption ($\Delta G_{H^*} \approx 0$), but insufficient Pt reserves and high cost make the wide use of Pt-based materials limited. Thus, many researchers have been intensively searching for the cost-effective alternatives to noble metal Pt. Before borides were really found to be promising HER catalysts, many nonprecious HER electrocatalysts had been explored, mainly including transition metal alloys (*e.g.*, NiMo, NiCu),[86,87] sulfides (*e.g.*, MoS_2, Ni_3S_2,

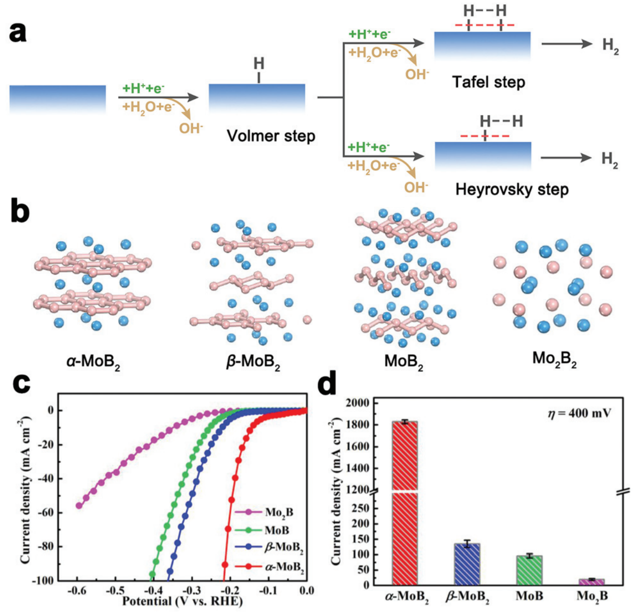

Fig. 12 (a) Schematic illustration of HER reaction pathways on the catalyst surface under acidic (green) and alkaline (red) conditions. (b) Crystal structures of α-MoB_2, β-MoB_2, MoB and Mo_2B. Mo atoms and B atoms are in blue and pink, respectively. (c) Linear sweep voltammetry (LSV) curves of the HER over α-MoB_2, β-MoB_2, MoB and Mo_2B in 0.5 M H_2SO_4 solution. (d) Comparison of the electrocatalytic activities of α-MoB_2, β-MoB_2, MoB and Mo_2B toward the HER. Reproduced with permission from ref. 48. Copyright 2017 the American Chemical Society.

Co_9S_8),[88–91] carbides (*e.g.*, Mo_2C, W_2C),[92–94] phosphides (*e.g.*, MoP, Ni_2P, CoP),[95–97] nitrides (*e.g.*, MoN, Ni_3N),[98,99] *etc.*

In this regard, commercially-available molybdenum boride (MoB) microparticles were first reported to be active HER catalysts with moderate catalytic activity by the group of Hu in 2012.[100] It was not until 2017 that Mo–B intermetallics as HER electrocatalysts attracted increasing attention. The research group led by Zou investigated the HER catalytic properties of four Mo–B phases with different crystal structures, including Mo_2B, MoB, α-MoB_2 and β-MoB_2 (Fig. 12b).[48] Their catalytic activities are found to decrease in the order of α-MoB_2 ≫ β-MoB_2 > MoB > Mo_2B (Fig. 12c and d). The α-MoB_2 catalyst was shown to exhibit a metallic conductivity. This material has a resistivity of $6.6 \pm 1.7 \times 10^{-7}$ Ω m, which is smaller than those of other Mo–B phases and a little larger than that of Pt (1.1×10^{-7} Ω m). In addition, as suggested by the theoretical results, the α-MoB_2 catalyst has a large density of efficient catalytic sites on both metal-terminated and boron-terminated surfaces for the HER. The distribution of active sites for α-MoB_2 is also suggested to be facet-independent. This property is not exhibited by the classic catalyst MoS_2, whose edges are the only catalytically active sites. Furthermore, the presence of graphene-like borophene subunits in α-MoB_2 is demonstrated to be a crucial factor responsible for the excellent electronic conductivity and catalytic activity. The boron content-dependent catalytic activities toward the HER for Mo–B phases were also identified by the Fokwa group simultaneously.[53,54,101,102]

The success of the MoB_2 catalyst encouraged researchers to investigate more transition metal diborides comprising the 3D metallic framework and 2D boron layers. Our group estimated the electrocatalytic activities for the HER on a family of twelve MB_2 (M = Ti, Zr, Hf, V, Nb, Ta, Cr, Mo, W, Re, Ru and Os) both theoretically and experimentally.[38] According to the theoretical results, both metal-terminated and boron-terminated surfaces in these MB_2 catalysts possess a high density of efficient catalytic sites for the HER. However, only the metal-terminated surfaces comply well with the experimental activity trends, indicating that the metal-terminated surfaces are main catalytic sites in real samples. This can be explained by two factors: (i) the metal-terminated surfaces are exposed facets in the as-prepared MB_2 samples; (ii) boron-terminated surfaces may be poisoned and thus lose the activity once exposed to air, because surface boron atoms have high oxophilicity. These MB_2 were found to present a general linear relationship between the catalytic activity and d-band center, indicating that the d-band center was a good descriptor to reflect HER catalytic activity (Fig. 13a). As suggested by the activity trends, RuB_2 is the most active material among these MB_2. RuB_2 is shown to have a higher theoretical activity than Pt due to little lower d-band center and smaller absolute value of ΔG_{H^*} than the former. In addition, the RuB_2 material has a high density of efficient sites, containing hollow site h and bridge sites b1 and b2, for catalyzing the HER (Fig. 13b). The experimental results further confirmed the HER activity of RuB_2 to be quite close to that of Pt/C in acidic solution, and even better than that of Pt/C in alkaline solution (Fig. 13c).

To understand the fundamental role of boron atoms in affecting the HER catalytic activity for boron-bearing intermetallics, our group studied the metal–boron electronic interaction in a class of fifteen transition metal monoborides.[41] They found strong orbital hybridization between boron sp

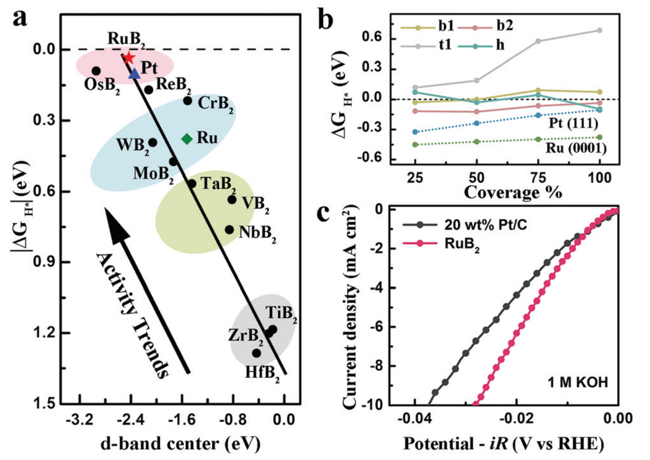

Fig. 13 (a) Fitted linear relationship between the adsorption free energy of atomic hydrogen (ΔG_{H^*}) and the d-band center of MB_2, Pt and Ru. (b) ΔG_{H^*} on the RuB_2(001), Ru(0001) and Pt(111) surface as a function of hydrogen coverage. (c) LSV curves for RuB_2 and 20 wt% Pt/C in 1.0 M KOH solution. Reproduced with permission from ref. 38. Copyright 2019 Wiley-VCH.

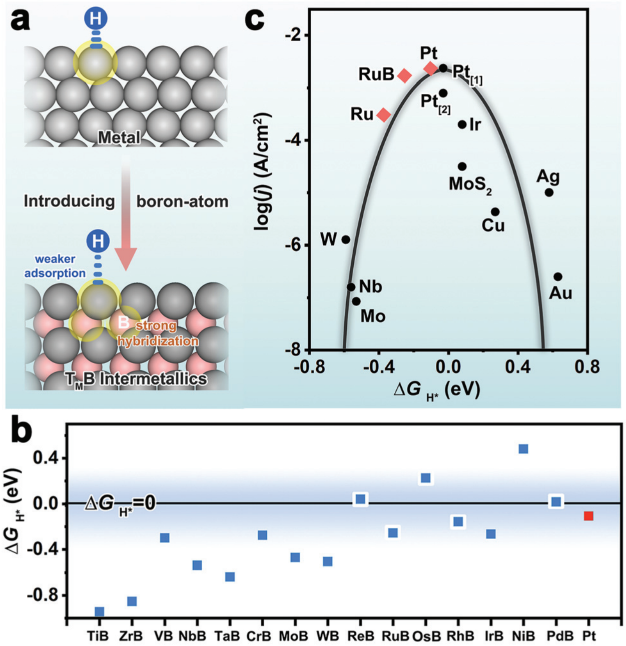

Fig. 14 (a) Schematic illustration of the influence of metal–boron orbital interaction on surface hydrogen adsorption properties in borides. (b) Calculated ΔG_{H^*} values of fifteen monoborides and Pt. (c) A volcano plot presenting the exchange current densities for the HER as a function of ΔG_{H^*} values for different materials. Reproduced with permission from ref. 41. Copyright 2020 Wiley-VCH.

states and metal d states, resulting in weaker surface H atom adsorption on metal-terminated borides compared to the corresponding pure metals (Fig. 14a). Taking RuB as an example, the Ru atom forms an octahedral field with the six surrounding B atoms on the basis of crystal field theory. The five-fold degeneracy of the ground state is split into three orbital singlets (*i.e.*, d_{z^2}, $d_{xz,yz}$, $d_{x^2-y^2,xy}$). The Ru $d_{xz,yz}$ orbitals are considered to strongly hybridize with B s–p orbitals (*i.e.*, ligand effect), resulting in broadening of the Ru d-band and downshift of the Ru d-band center (relative to the Fermi level). The more negative d-band center than metallic Ru is a crucial factor responsible for the lower hydrogen adsorption energy of RuB. In addition, given that the boron-induced crystal expansion (*i.e.*, strain effect) will reduce the Ru d-orbital overlap and bring about an upshift of the d-band center, the ligand effect is demonstrated to predominate over the strain effect in RuB. As suggested by the theoretical results, the modulation of metal d-band properties made several monoborides (such as RuB, PdB and ReB) possess suitable ΔG_{H^*} values close to Pt (Fig. 14b). Furthermore, the Pt-like catalytic activity toward the HER of RuB was experimentally identified by the authors (Fig. 14c).

Our group comparatively investigated the HER catalytic activities of four Ru–B intermetallics with different crystal structures, including Ru_7B_3, RuB, Ru_2B_3 and RuB_2.[42] The HER activities of RuB, Ru_2B_3 and RuB_2 are close to that of Pt in acidic solution and little better than that of Pt in alkaline solution, while Ru_7B_3 has a moderate activity similar to metallic Ru. Among them, the RuB_2 material exhibits not only the optimal HER activity, but also the best stability in both acidic and alkaline solutions. Their different catalytic activities are found to depend on the diverse crystal phases, which produce distinct catalytic surfaces. The existence of a boat-like boron sheet in RuB_2 is demonstrated to be a crucial structural motif fragment responsible for the excellent catalytic activity.

Besides Ru–B phase catalysts, the borides of palladium were also considered as alternative catalysts to platinum. Liu's group calculated the formation energy of a range of Pd–B alloys, and found the most stable crystal phase transforming from face-centered (fcc) to hexagonal close packing (hcp) after the incorporation of B atoms.[103,104] The hcp Pd_2B phase was identified as the thermodynamically most stable Pd–B phase. As suggested by the theoretical results, the fcc-to-hcp phase transition significantly facilitated B diffusion in the Pd_2B lattice. The Pd_2B phase was predicted to have higher intrinsic activity than Pt for the HER, because the presence of subsurface boron atoms and the expansion of crystal lattice in the Pd_2B phase promote the Tafel step (*i.e.*, $H^* + H^* \rightarrow H_2$) for the HER. To validate the theoretical results, the research group prepared Pd_2B nanosheets with a solvothermal approach, and achieved higher catalytic activity than commercial Pt/C toward the HER. We should note that the crystal structure of the as-prepared sample mismatches with that used for theoretical calculation, because its X-ray diffraction (XRD) patterns are consistent with those of the hcp Pd phase (probably B-doped Pd), rather than structurally ordered intermetallic Pd_2B.

Some design strategies for improving the HER performances have been developed. Alameda *et al.* obtained MoAlB sheets by partial etching Al from MoAlB powders in alkaline solution.[105] The etched MoAlB presented significantly improved HER activity due to the increase of exposed active sites after etching. Dutta *et al.* proposed an orthorhombic Co_2MoB_4 material comprising double boron chains as HER electrocatalysts, and developed a Ni incorporation strategy to enhance HER activity.[106] The introduction of Ni atoms not only improved electrical conductivity, but also favored the hydrogen adsorption on Mo active sites. The Ni doping strategy was also applied to promote the intrinsic HER properties of WB_2 through optimizing its electronic structure on the catalytically active surface.[71] Zhuang *et al.* enhanced the HER catalytic activity of MoB by constructing a Schottky junction between n-type semiconductor $g\text{-}C_3N_4$ and metallic MoB.[107] The superior activity of the Schottky catalyst is because enriched electron density in the MoB surface lowers the kinetic barrier for the HER.

4.2. Electrocatalytic OER

The oxygen evolution reaction (OER) often serves as the anodic half-reaction in many useful electrochemical processes, including water splitting, CO_2 reduction and N_2 reduction, and thus is of great importance.[108,109] However, the OER proceeds through a four-electron transfer pathway and involves multiple oxygen-containing intermediates (OH, O and OOH), leading to

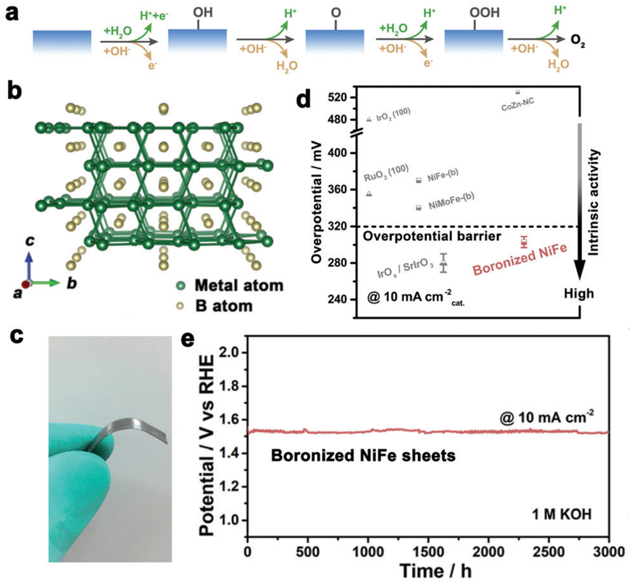

Fig. 15 (a) Schematic illustration of OER reaction pathways on the catalyst surface under acidic (green) and alkaline (red) conditions. (b) Crystal structure of M_2B. (c) Digital image of boronized metal sheets. (d) Comparison of intrinsic catalytic activities between boronized NiFe sheets and some reported representative electrocatalysts towards OER. (e) Chronopotentiometric curve of boronized NiFe sheets at a current density of 10 mA cm^{-2} in 1 M KOH solution. Reproduced with permission from ref. 44. Copyright 2019 Royal Society of Chemistry.

sluggish kinetics (Fig. 15a). RuO_2 and IrO_2 are traditional OER electrocatalysts with high activity, but their poor durability during catalysis and scarcity in nature restrict their large-scale applications.[110–112] Therefore, extensive efforts have been devoted to discovering nonprecious OER electrocatalysts (based on Ni, Fe, Co, Mn, *etc.*) to replace the Ir-/Ru-based catalysts. Over the past decade, many nonprecious materials as efficient OER electrocatalysts have been reported, mainly containing layered double hydroxides,[113–115] perovskite oxides,[116–119] spinel oxides,[120–122] multi-metallic mixed oxides,[123–125] and non-oxide-derived compounds.[126–129]

Transition metal borides as a class of non-oxide OER electrocatalysts received much attention in recent years. Particularly some metal-rich borides exhibited promising OER activity, mainly including cobalt borides (*e.g.*, Co_2B, Co_3B),[130,131] iron borides (*e.g.*, Fe_2B),[132] nickel borides (*e.g.*, Ni_2B, Ni_3B),[45,133] and their solid solutions (*e.g.*, $Ni_xFe_{2-x}B$).[134] For example, our group performed a boronizing treatment on diverse metal sheets (including Fe, Co, Ni, NiFe alloys and steel sheets) to produce M_2B layers on the corresponding metal sheets as oxygen evolution electrodes (Fig. 15b and c).[44] Metal atoms bond together in M_2B to form a 3D metal framework, while boron atoms reside in the voids of the framework with M–B bonds. The OER catalytic activities of the boronized metal sheets were found to have the same trends as that of the corresponding metal sheets (Ni > Co > Fe). The boronized metal sheets presented an order of magnitude higher OER activities than the corresponding metal sheets. The boronized NiFe alloy sheets showed outstanding intrinsic catalytic activity better than the state-of-the-art catalysts, and conquered the overpotential barrier of 320 mV to generate a current density of 10 mA $cm_{catalyst}^{-2}$ (Fig. 15d). The boronized NiFe electrodes can remain highly stable for more than 3000 hours in 1 M KOH solution (Fig. 15e). Furthermore, the boronized NiFe sheets and boronized steel sheets simultaneously possessed high activity, high stability and outstanding corrosion resistance toward the OER in 30% KOH solution, a widely used electrolyte for commercial alkaline water electrolysis.

Although metal boride catalysts present attractive catalytic properties, the derived active phases during the OER catalytic process still maintain poorly understood. Some investigators declare that catalytically active phases in boride catalysts are the metal oxyhydroxides, while others consider that they possess a similar structure and function to the reported Ni–B_i film, in complete ignorance of the effect of boron. Taking boronized Ni sheet as an example, our group found that the amorphous, ultrathin layers (2–5 nm) were generated on the electrode surface after the OER.[44,45] Metaborate was demonstrated to be the stable boron species in the surface oxidized layers, while the electrode surface was oxidized and transformed into γ-NiOOH during the catalysis process. As a result, metaborate-containing oxyhydroxide films formed *in situ* on the boride surfaces were identified as the catalytic phase with high OER activity. The authors found that the metaborate species-induced electron redistribution could increase the electron density of Ni atoms in the thin NiOOH layer. The modified electronic properties of NiOOH were proposed to optimize the binding strength of oxygen intermediates and improve the OER activity.

Some ternary borides were also reported to be active for the OER. For example, Mann *et al.* proposed a layered-structure boride $AlFe_2B_2$ as an efficient pre-electrocatalyst for the OER under alkaline conditions.[135] During electrochemical OER testing, Al atoms were partially leached from $AlFe_2B_2$, resulting in exposed $[Fe_2B_2]$ layers decorated with the Fe_3O_4 nanoclusters as active sites. The resulting catalysts exhibited high catalytic activity, and maintained high catalytic stability for over ten days. Despite these advances, our understanding on how boride catalysts work during the OER process is still limited. More efforts should be made to explore electronic structure-OER activity relationships for unraveling the activity origin of borides.

4.3. Electrocatalytic NRR

Compared to the HER and OER, researchers show relatively less interest in developing metal borides for the electrocatalytic nitrogen reduction reaction (NRR). The ammonia synthesis through the electrocatalytic NRR has emerged as a current hot topic in catalysis because the reaction is an attractive alternative to the Haber–Bosch process, an industrial ammonia synthesis approach with heavy CO_2 emissions and energy consumption.[136] The NRR involves two possible reaction pathways (*i.e.*, dissociative and associative pathways) to undergo the formation and conversion of different

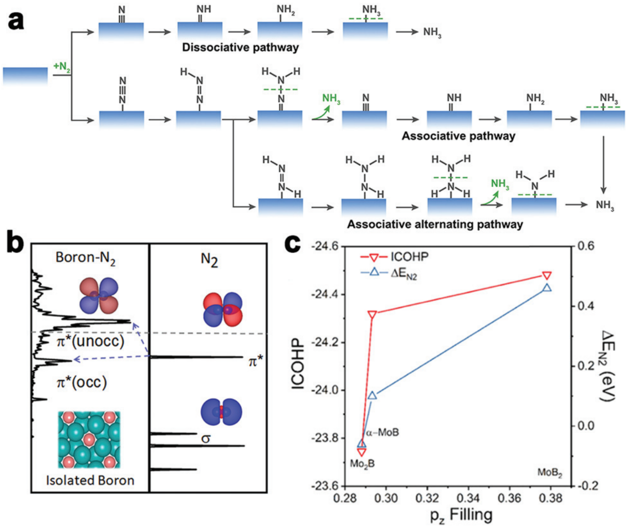

Fig. 16 (a) Schematic illustration of NRR reaction pathways on the catalyst surface. (b) Schematic illustrations of hybridization interactions between the boron p-orbital of Mo_2B and the π*-orbital of the N_2 molecule. (c) Correlation between p_z-orbital filling with ICOHP and adsorption energy of N_2. Reproduced with permission from ref. 46. Copyright 2020 the American Chemical Society.

N-containing intermediates (Fig. 16a).[137] High performance electrocatalysts are desired to activate and convert N_2 to NH_3.

In order to explore the NRR activity on metal borides, Qiao's group recently modeled several molybdenum boride catalysts (Mo_2B, α-MoB, and MoB_2) toward the NRR.[46] The binding strength of N_2 was found to depend on the occupation of hybridized orbitals between the p-orbital of the boron site and the antibonding π*-orbital of N_2 (Fig. 16b). The filling of p_z-orbital could serve as a descriptor of N_2 activation (indicated by the ICOHP result). In diverse Mo–B phases, the p_z filling increased with the increase of the boron content (Fig. 16c). The Mo_2B phase containing an isolated boron site has less filling of the p_z-orbital, thus benefiting the activation of N_2. They also extended the research to more M_2B (M = Ti, Cr, Mn, Fe, Co, Ni, Ta, and W) with an isolated boron site. As suggested by the theoretical results, Co_2B and Fe_2B were screened as potential candidates for the NRR because of their moderate filling of the p_z-orbital and adsorption strength of reaction intermediates.

Using first principles calculations, Qin *et al.* calculated the binding energies of several MB_2 (TM = Ti, V, Cr, Mn, Nb and Mo) interacting with N_2, NH_3 and H_2O, and selected TiB_2, VB_2 and NbB_2 as potential candidates.[137] The authors further considered VB_2 as the most efficient electrocatalyst after investigating two possible NRR mechanisms. Another theoretical study of NRR based on iron borides demonstrated that β-FeB_6 with an optimal free energy change for elementary steps gave the best performance among four different phases (FeB, FeB_2, α-FeB_6, and β-FeB_6).[138] The active site for the NRR was identified to be the lightly oxidized iron site. The above theoretical results provide the design principle to prepare highly active electrocatalysts for the NRR.

5. Conclusions and outlook

In this article, we have reviewed the recent achievements in the synthesis of phase-pure, well-defined intermetallic borides, and their emerging electrocatalytic applications toward various reactions. The important roles of boron atoms in the modulation of surface catalytic properties make intermetallic borides indispensable constituents in the electrocatalytic process. The potential applications of borides can also be extended to a wide range including Li-ion batteries,[139] supercapacitors,[140] photocatalysis,[141] and other catalytic reactions, such as CO_2 reduction and $NaBH_4$ hydrolysis.[142,143] Despite the great achievements made in the synthesis and catalytic properties of intermetallic borides, as mentioned in the review, several challenges should still be addressed for future advancement. (i) Most as-prepared, crystallized borides have uncontrollable morphology and low specific surface areas, which is not favorable for exposing the high density of catalytically active sites. Therefore, more research works for precisely controlling the particle size and morphology of borides are called for. (ii) The combination of a metal with boron probably forms into several boride phases with distinct stoichiometries and crystal structures, but it prefers to produce the most stable phase rather than other metastable phases during chemical synthesis. So, it is necessary to expand the synthetic route for selectively synthesizing the target metastable phases. (iii) The chemical properties of borides, such as chemical stability in air (or water) and acid/alkali resistance, are of vital importance to catalytic applications, especially electrocatalysis working in the electrolyte. However, knowledge about this is scant and unsystematic, and further research and summarization is required. (iv) Current synthesis and catalytic studies of metal borides mainly focus on binary borides which only account for less than 20% of the metal–boron system, while studies on multiple borides are scarce. It is necessary to explore the preparative method of ternary, quaternary or larger systems, and investigate their catalytic applications. (v) If compared with amorphous boride catalysts, the well-defined boride catalysts reviewed in this article are far from being actively explored. More studies for establishing a standardized testing and catalytic mechanism on borides need to be performed.

Conflicts of interest

There are no conflicts to declare.

Acknowledgements

X. Zou is thankful for the financial support from the National Natural Science Foundation of China (NSFC): Grant No. 21922507 and 21771079 and the Fok Ying Tung Education Foundation: Grant No. 161011. H. Chen acknowledges the financial support from the NSFC (Grant No. 21901083), the Postdoctoral Innovative Talent Support Program (Grant No.

BX20180120) and the China Postdoctoral Science Foundation (Grant No. 2018M641771). We also thank the National Natural Science Foundation of China (Grant No. 21621001) and the 111 Project (No. B17020) for financial support.

References

1 R. Nesper, Bonding patterns in intermetallic compounds, *Angew. Chem., Int. Ed. Engl.*, 1991, **30**, 789–817.

2 G. Akopov, M. T. Yeung and R. B. Kaner, Rediscovering the crystal chemistry of borides, *Adv. Mater.*, 2017, **29**, 1604506.

3 F. Jones and R. Taylor, On boron hydride, *J. Chem. Soc.*, 1881, **39**, 213–219.

4 F. Jones, On a hydride of boron, *J. Chem. Soc.*, 1879, **35**, 41–42.

5 F. E. Weston and H. R. Ellis, Note on the action of aluminium powder on silica and boric anhydride, *Trans. Faraday Soc.*, 1908, **3**, 170–176.

6 R. Kiessling, The borides of some transition elements, *J. Electrochem. Soc.*, 1951, **98**, 166.

7 N. Greenwood, R. Parish and P. Thornton, Metal borides, *Q. Rev., Chem. Soc.*, 1966, **20**, 441–464.

8 N. Greenwood, R. Parish and P. Thornton, Some reactions of metal borides, *J. Chem. Soc.*, 1965, 545–549.

9 V. I. Matkovich, *Boron and refractory borides*, Springer-Verlag, Berlin, 1977.

10 B. P. Fokwa, Borides: solid-state chemistry, *Encycl. Inorg. Bioinorg. Chem.*, 2014, 1–14.

11 V. Babizhetskyy, J. Bauer, R. Gautier, K. Hiebl, A. Simon and J.-F. Halet, in *Handbook on the Physics and Chemistry of Rare Earths*, ed. J.-C. G. Bünzli and V. K. Pecharsky, Elsevier, 2018, vol. 53, pp. 145–269.

12 P. Shankhari, N. G. Bakshi, Y. Zhang, D. Stekovic, M. E. Itkis and B. P. T. Fokwa, A delicate balance between antiferromagnetism and ferromagnetism: theoretical and experimental studies of $A_2MRu_5B_2$ (A = Zr, Hf; M = Fe, Mn) metal borides, *Chem. – Eur. J.*, 2020, **26**, 1979–1988.

13 J. P. Scheifers, Y. Zhang and B. P. Fokwa, Boron: enabling exciting metal-rich structures and magnetic properties, *Acc. Chem. Res.*, 2017, **50**, 2317–2325.

14 B. Albert and H. Hillebrecht, Boron: elementary challenge for experimenters and theoreticians, *Angew. Chem., Int. Ed.*, 2009, **48**, 8640–8668.

15 J. Hulm and B. Matthias, New superconducting borides and nitrides, *Phys. Rev.*, 1951, **82**, 273.

16 G. F. Hardy and J. K. Hulm, The superconductivity of some transition metal compounds, *Phys. Rev.*, 1954, **93**, 1004.

17 J. Nagamatsu, N. Nakagawa, T. Muranaka, Y. Zenitani and J. Akimitsu, Superconductivity at 39 K in magnesium diboride, *Nature*, 2001, **410**, 63–64.

18 R. B. Kaner, J. J. Gilman and S. H. Tolbert, Designing superhard materials, *Science*, 2005, **308**, 1268–1269.

19 H.-Y. Chung, M. B. Weinberger, J. B. Levine, A. Kavner, J.-M. Yang, S. H. Tolbert and R. B. Kaner, Synthesis of ultra-incompressible superhard rhenium diboride at ambient pressure, *Science*, 2007, **316**, 436–439.

20 R. Mohammadi, M. Xie, A. T. Lech, C. L. Turner, A. Kavner, S. H. Tolbert and R. B. Kaner, Toward inexpensive superhard materials: tungsten tetraboride-based solid solutions, *J. Am. Chem. Soc.*, 2012, **134**, 20660–20668.

21 G. Akopov, M. T. Yeung, C. L. Turner, R. Mohammadi and R. B. Kaner, Extrinsic hardening of superhard tungsten tetraboride alloys with group 4 transition metals, *J. Am. Chem. Soc.*, 2016, **138**, 5714–5721.

22 H. Gou, N. Dubrovinskaia, E. Bykova, A. A. Tsirlin, D. Kasinathan, W. Schnelle, A. Richter, M. Merlini, M. Hanfland, A. M. Abakumov, D. Batuk, G. Van Tendeloo, Y. Nakajima, A. N. Kolmogorov and L. Dubrovinsky, Discovery of a superhard iron tetraboride superconductor, *Phys. Rev. Lett.*, 2013, **111**, 157002.

23 J. Herbst, $R_2Fe_{14}B$ materials: Intrinsic properties and technological aspects, *Rev. Mod. Phys.*, 1991, **63**, 819.

24 S. Gabani, K. Flachbart, K. Siemensmeyer and T. Mori, Magnetism and superconductivity of rare earth borides, *J. Alloys Compd.*, 2020, **821**, 153201.

25 X. Tan, P. Chai, C. M. Thompson and M. Shatruk, Magnetocaloric effect in $AlFe_2B_2$: toward magnetic refrigerants from earth-abundant elements, *J. Am. Chem. Soc.*, 2013, **135**, 9553–9557.

26 M. Gürsoy, M. Takeda and B. Albert, High-pressure densified solid solutions of alkaline earth hexaborides (Ca/Sr, Ca/Ba, Sr/Ba) and their high-temperature thermoelectric properties, *J. Solid State Chem.*, 2015, **221**, 191–195.

27 A. Sussardi, T. Tanaka, A. U. Khan, L. Schlapbach and T. Mori, Enhanced thermoelectric properties of samarium boride, *J. Materiomics*, 2015, **1**, 196–204.

28 T. Mori, T. Nishimura, W. Schnelle, U. Burkhardt and Y. Grin, The origin of the n-type behavior in rare earth borocarbide $Y_{1-x}B_{28.5}C_4$, *Dalton Trans.*, 2014, **43**, 15048–15054.

29 C. Wu, H. Huang, W. Lu, Z. Wei, X. Ni, F. Sun, P. Qing, Z. Liu, J. Ma, W. Wei, L. Chen, C. Yan and L. Mai, Mg doped Li-LiB alloy with in situ formed lithiophilic LiB skeleton for lithium metal batteries, *Adv. Sci.*, 2020, **7**, 201902643.

30 Q. Pang, C. Y. Kwok, D. Kundu, X. Liang and L. Nazar, Lightweight metallic MgB_2 mediates polysulfide redox and promises high-energy-density lithium-sulfur batteries, *Joule*, 2019, **3**, 136–148.

31 C. Li, X. Liu, L. Zhu, R. Huang, M. Zhao, L. Xu and Y. Qian, Conductive and polar titanium boride as a sulfur host for advanced lithium-sulfur batteries, *Chem. Mater.*, 2018, **30**, 6969–6977.

32 B. Guan, Y. Zhang, L. Fan, X. Wu, M. Wang, Y. Qiu, N. Zhang and K. Sun, Blocking polysulfide with Co_2B@CNT via "synergetic adsorptive effect" toward ultra-high-rate capability and robust lithium-sulfur battery, *ACS Nano*, 2019, **13**, 6742–6750.

33 R. Paul, P. Buisson and N. Joseph, Catalytic activity of nickel borides, *Ind. Eng. Chem.*, 1952, **44**, 1006–1010.

34 B. Ganem and J. O. Osby, Synthetically useful reactions with metal boride and aluminide catalysts, *Chem. Rev.*, 1986, **86**, 763–780.

35 S. Carenco, D. Portehault, C. Boissiere, N. Mezailles and C. Sanchez, Nanoscaled metal borides and phosphides: recent developments and perspectives, *Chem. Rev.*, 2013, **113**, 7981–8065.

36 M. Lewandowski, Hydrotreating activity of bulk NiB alloy in model reaction of hydrodenitrogenation of carbazole, *Appl. Catal., B*, 2015, **168**, 322–332.

37 P. K. Singh and T. Das, Generation of hydrogen from $NaBH_4$ solution using metal-boride (CoB, FeB, NiB) catalysts, *Int. J. Hydrogen Energy*, 2017, **42**, 29360–29369.

38 Q. Li, X. Zou, X. Ai, H. Chen, L. Sun and X. Zou, Revealing activity trends of metal diborides toward ph-universal hydrogen evolution electrocatalysts with Pt-like activity, *Adv. Energy Mater.*, 2019, **9**, 1803369.

39 T. Mori, Thermoelectric and magnetic properties of rare earth borides: boron cluster and layered compounds, *J. Solid State Chem.*, 2019, **275**, 70–82.

40 T. Mori, in *Handbook on the Physics and Chemistry of Rare Earths*, ed. K. A. Gschneidner, J.-C. G. Bünzli and V. K. Pecharsky, Elsevier, 2008, vol. 38, pp. 105–173.

41 X. Ai, X. Zou, H. Chen, Y. Su, X. Feng, Q. Li, Y. Liu, Y. Zhang and X. Zou, Transition-metal-boron intermetallics with strong interatomic d-sp orbital hybridization for high-performance electrocatalysis, *Angew. Chem., Int. Ed.*, 2020, **59**, 3961–3965.

42 X. Zou, L. Wang, X. Ai, H. Chen and X. Zou, Crystal phase-dependent electrocatalytic hydrogen evolution performance of ruthenium-boron intermetallics, *Chem. Commun.*, 2020, **56**, 3061–3064.

43 Q. Xu, Y. Liu, H. Jiang, Y. Hu, H. Liu and C. Li, Unsaturated sulfur edge engineering of strongly coupled MoS_2 nanosheet-carbon macroporous hybrid catalyst for enhanced hydrogen generation, *Adv. Energy Mater.*, 2019, **9**, 1802553.

44 F. Guo, Y. Wu, H. Chen, Y. Liu, L. Yang, X. Ai and X. Zou, High-performance oxygen evolution electrocatalysis by boronized metal sheets with self-functionalized surfaces, *Energy Environ. Sci.*, 2019, **12**, 684–692.

45 J. Li, H. Chen, Y. Liu, R. Gao and X. Zou, In situ structural evolution of a nickel boride catalyst: synergistic geometric and electronic optimization for the oxygen evolution reaction, *J. Mater. Chem. A*, 2019, **7**, 5288–5294.

46 X. Liu, Y. Jiao, Y. Zheng and S.-Z. Qiao, Isolated boron sites for electroreduction of dinitrogen to ammonia, *ACS Catal.*, 2020, **10**, 1847–1854.

47 B. Sun, X. Jia, J. Zhao, Y. Li, H. Liu and H. Ma, Effects of pressure on the microstructure and simultaneous optimization of the electrical and thermal transport properties of $Yb_{0.5}Ba_{7.5}Ga_{16}Ge_{30}$, *Inorg. Chem.*, 2018, **57**, 3323–3328.

48 Y. Chen, G. Yu, W. Chen, Y. Liu, G.-D. Li, P. Zhu, Q. Tao, Q. Li, J. Liu, X. Shen, H. Li, X. Huang, D. Wang, T. Asefa and X. Zou, Highly active, nonprecious electrocatalyst comprising borophene subunits for the hydrogen evolution reaction, *J. Am. Chem. Soc.*, 2017, **139**, 12370–12373.

49 Q. Tao, D. Zheng, X. Zhao, Y. Chen, Q. Li, Q. Li, C. Wang, T. Cui, Y. Ma, X. Wang and P. Zhu, Exploring hardness and the distorted sp^2 hybridization of B-B bonds in WB_3, *Chem. Mater.*, 2014, **26**, 5297–5302.

50 S. Ma, K. Bao, Q. Tao, P. Zhu, T. Ma, B. Liu, Y. Liu and T. Cui, Manganese mono-boride, an inexpensive room temperature ferromagnetic hard material, *Sci. Rep.*, 2017, **7**, 43759.

51 S. Ma, K. Bao, Q. Tao, C. Xu, X. Feng, X. Zhao, Y. Ge, P. Zhu and T. Cui, Double-zigzag boron chain-enhanced Vickers hardness and manganese bilayers-induced high d-electron mobility in Mn_3B_4, *Phys. Chem. Chem. Phys.*, 2019, **21**, 2697–2705.

52 H. Tang, X. Gao, J. Zhang, B. Gao, W. Zhou, B. Yan, X. Li, Q. Zhang, S. Peng, D. Huang, L. Zhang, X. Yuan, B. Wan, C. Peng, L. Wu, D. Zhang, H. Liu, L. Gu, F. Gao, T. Irifune, R. Ahuja, H.-K. Mao and H. Gou, Boron-rich molybdenum boride with unusual short-range vacancy ordering, anisotropic hardness, and superconductivity, *Chem. Mater.*, 2020, **32**, 459–467.

53 H. Park, A. Encinas, J. P. Scheifers, Y. Zhang and B. P. T. Fokwa, Boron-dependency of molybdenum boride electrocatalysts for the hydrogen evolution reaction, *Angew. Chem., Int. Ed.*, 2017, **56**, 5575–5578.

54 H. Park, Y. Zhang, J. P. Scheifers, P. R. Jothi, A. Encinas and B. P. T. Fokwa, Graphene- and phosphorene-like boron layers with contrasting activities in highly active Mo_2B_4 for hydrogen evolution, *J. Am. Chem. Soc.*, 2017, **139**, 12915–12918.

55 S. Otani and T. Mori, Flux growth and magnetic properties of CaB_6 crystals, *J. Phys. Soc. Jpn.*, 2002, **71**, 1791–1792.

56 W. Du, D. Xu, H. Zhang, X. Wang, G. Zhang, X. Hou, H. Liu and Y. Wang, Single crystal growth of MgB_2 by using Mg-self-flux method at ambient pressure, *J. Cryst. Growth*, 2004, **268**, 123–127.

57 M. Belyansky and M. Trenary, heteroepitaxy of hafnium diboride on a hafnium(0001) single crystal surface, *Chem. Mater.*, 1997, **9**, 403–405.

58 S. S. Amin, S.-Y. Li, J. R. Roth and T. T. Xu, Single crystalline alkaline-earth metal hexaboride one-dimensional (1D) nanostructures: synthesis and characterization, *Chem. Mater.*, 2009, **21**, 763–770.

59 P. Peshev, A thermodynamic estimation of the chemical vapor deposition of some borides, *J. Solid State Chem.*, 2000, **154**, 157–161.

60 J. M. V. Nsanzimana, Y. Peng, Y. Y. Xu, L. Thia, C. Wang, B. Y. Xia and X. Wang, An efficient and earth-abundant oxygen-evolving electrocatalyst based on amorphous metal borides, *Adv. Energy Mater.*, 2018, **8**, 1701475.

61 L. Wang, J. Li, X. Zhao, W. Hao, X. Ma, S. Li and Y. Guo, Surface-activated amorphous iron borides (Fe_xB) as efficient electrocatalysts for oxygen evolution reaction, *Adv. Mater. Interfaces*, 2019, **6**, 1801690.

62 J. M. V. Nsanzimana, L. Gong, R. Dangol, V. Reddu, V. Jose, B. Y. Xia, Q. Yan, J.-M. Lee and X. Wang, Tailoring of metal boride morphology via anion for efficient water oxidation, *Adv. Energy Mater.*, 2019, **9**, 1901503.

63 J. Masa, I. Sinev, H. Mistry, E. Ventosa, M. de la Mata, J. Arbiol, M. Muhler, B. Roldan Cuenya and W. Schuhmann, Ultrathin high surface area nickel boride (Ni_xB) nanosheets as highly efficient electrocatalyst for oxygen evolution, *Adv. Energy Mater.*, 2017, **7**, 1700381.

64 Y. Li, B. Huang, Y. Sun, M. Luo, Y. Yang, Y. Qin, L. Wang, C. Li, F. Lv, W. Zhang and S. Guo, Multimetal borides nanochains as efficient electrocatalysts for overall water splitting, *Small*, 2019, **15**, 1804212.

65 W. Hao, R. Wu, R. Zhang, Y. Ha, Z. Chen, L. Wang, Y. Yang, X. Ma, D. Sun, F. Fang and Y. Guo, Electroless plating of highly efficient bifunctional boride-based electrodes toward practical overall water splitting, *Adv. Energy Mater.*, 2018, **8**, 1801372.

66 N. Xu, G. Cao, Z. Chen, Q. Kang, H. Dai and P. Wang, Cobalt nickel boride as an active electrocatalyst for water splitting, *J. Mater. Chem. A*, 2017, **5**, 12379–12384.

67 D. Portehault, S. Devi, P. Beaunier, C. Gervais, C. Giordano, C. Sanchez and M. Antonietti, A general solution route toward metal boride nanocrystals, *Angew. Chem., Int. Ed.*, 2011, **50**, 3262–3265.

68 A. Aprea, A. Maspero, A. F. Albisetti and G. Giunchi, Synthesis of alkaline-earth hexaborides, MB_6 (M = Ca, Ba, Sr), by a solid state metathesis (SSM) reaction, *Solid State Sci.*, 2012, **14**, 1587–1590.

69 A. J. Lupinetti, J. L. Fife, E. Garcia, P. K. Dorhout and K. D. Abney, Low-temperature synthesis of uranium tetraboride by solid-state metathesis reactions, *Inorg. Chem.*, 2002, **41**, 2316–2318.

70 E. G. Gillan and R. B. Kaner, Synthesis of refractory ceramics via rapid metathesis reactions between solid-state precursors, *Chem. Mater.*, 1996, **8**, 333–343.

71 F. Guo, Y. Wu, X. Ai, H. Chen, G.-D. Li, W. Chen and X. Zou, A class of metal diboride electrocatalysts synthesized by a molten salt-assisted reaction for the hydrogen evolution reaction, *Chem. Commun.*, 2019, **55**, 8627–8630.

72 S. Okada, T. Shishido, T. Mori, K. Iizumi, K. Kudou and K. Nakajima, Crystal growth of $MgAlB_{14}$-type compounds using metal salts and some properties, *J. Alloys Compd.*, 2008, **458**, 297–301.

73 X. Wang, G. Tai, Z. Wu, T. Hu and R. Wang, Ultrathin molybdenum boride films for highly efficient catalysis of the hydrogen evolution reaction, *J. Mater. Chem. A*, 2017, **5**, 23471–23475.

74 P. R. Jothi, K. Yubuta and B. P. T. Fokwa, A simple, general synthetic route toward nanoscale transition metal borides, *Adv. Mater.*, 2018, **30**, 1704181.

75 H. Chen, X. Ai, W. Liu, Z. Xie, W. Feng, W. Chen and X. Zou, Promoting subordinate, efficient ruthenium sites with interstitial silicon for Pt-like electrocatalytic activity, *Angew. Chem., Int. Ed.*, 2019, **58**, 11409–11413.

76 H. Jin, C. Guo, X. Liu, J. Liu, A. Vasileff, Y. Jiao, Y. Zheng and S.-Z. Qiao, Emerging two-dimensional nanomaterials for electrocatalysis, *Chem. Rev.*, 2018, **118**, 6337–6408.

77 M. Khazaei, J. Wang, M. Estili, A. Ranjbar, S. Suehara, M. Arai, K. Esfarjani and S. Yunoki, Novel MAB phases and insights into their exfoliation into 2D MBenes, *Nanoscale*, 2019, **11**, 11305–11314.

78 L. T. Alameda, P. Moradifar, Z. P. Metzger, N. Alem and R. E. Schaak, Topochemical deintercalation of Al from MoAlB: stepwise etching pathway, layered intergrowth structures, and two-dimensional mbene, *J. Am. Chem. Soc.*, 2018, **140**, 8833–8840.

79 J. Wang, T.-N. Ye, Y. Gong, J. Wu, N. Miao, T. Tada and H. Hosono, Discovery of hexagonal ternary phase Ti_2InB_2 and its evolution to layered boride TiB, *Nat. Commun.*, 2019, **10**, 2284.

80 H. Zhang, H. Xiang, F.-Z. Dai, Z. Zhang and Y. Zhou, First demonstration of possible two-dimensional mbene CrB derived from MAB phase Cr_2AlB_2, *J. Mater. Sci. Technol.*, 2018, **34**, 2022–2026.

81 H. Zhang, F.-Z. Dai, H. Xiang, X. Wang, Z. Zhang and Y. Zhou, Phase pure and well crystalline Cr_2AlB_2: A key precursor for two-dimensional CrB, *J. Mater. Sci. Technol.*, 2019, **35**, 1593–1600.

82 W. Xiao, W. Lei, M. Gong, H. L. Xin and D. Wang, Recent advances of structurally ordered intermetallic nanoparticles for electrocatalysis, *ACS Catal.*, 2018, **8**, 3237–3256.

83 S. Furukawa and T. Komatsu, Intermetallic compounds: promising inorganic materials for well-structured and electronically modified reaction environments for efficient catalysis, *ACS Catal.*, 2017, **7**, 735–765.

84 L. Rößner and M. Armbrüster, Electrochemical Energy conversion on intermetallic compounds: a review, *ACS Catal.*, 2019, **9**, 2018–2062.

85 X. Zou and Y. Zhang, Noble metal-free hydrogen evolution catalysts for water splitting, *Chem. Soc. Rev.*, 2015, **44**, 5148–5180.

86 Y. Shen, Y. Zhou, D. Wang, X. Wu, J. Li and J. Xi, Nickel-copper alloy encapsulated in graphitic carbon shells as electrocatalysts for hydrogen evolution reaction, *Adv. Energy Mater.*, 2018, **8**, 1701759.

87 Y. Ito, T. Ohto, D. Hojo, M. Wakisaka, Y. Nagata, L. Chen, K. Hu, M. Izumi, J.-I. Fujita and T. Adschiri, Cooperation between holey graphene and NiMo alloy for hydrogen evolution in an acidic electrolyte, *ACS Catal.*, 2018, **8**, 3579–3586.

88 T. F. Jaramillo, K. P. Jørgensen, J. Bonde, J. H. Nielsen, S. Horch and I. Chorkendorff, Identification of active edge sites for electrochemical H_2 evolution from MoS_2 nanocatalysts, *Science*, 2007, **317**, 100–102.

89 L.-L. Feng, G. Yu, Y. Wu, G.-D. Li, H. Li, Y. Sun, T. Asefa, W. Chen and X. Zou, High-index faceted Ni_3S_2 nanosheet arrays as highly active and ultrastable electrocatalysts for water splitting, *J. Am. Chem. Soc.*, 2015, **137**, 14023–14026.

90 L.-L. Feng, G.-D. Li, Y. Liu, Y. Wu, H. Chen, Y. Wang, Y.-C. Zou, D. Wang and X. Zou, Carbon-armored Co_9S_8 nanoparticles as All-pH efficient and durable H_2-evolving electrocatalysts, *ACS Appl. Mater. Interfaces*, 2015, **7**, 980–988.

91 S. Liu, M. Tong, G. Liu, X. Zhang, Z. Wang, G. Wang, W. Cai, H. Zhang and H. Zhao, S,N-containing Co-MOF derived Co_9S_8@S, N-doped carbon materials as efficient oxygen electrocatalysts and supercapacitor electrode materials, *Inorg. Chem. Front.*, 2017, **4**, 491–498.

92 Y. Liu, G. Yu, G. D. Li, Y. Sun, T. Asefa, W. Chen and X. Zou, Coupling Mo_2C with nitrogen-rich nanocarbon leads to efficient hydrogen-evolution electrocatalytic sites, *Angew. Chem., Int. Ed.*, 2015, **54**, 10752–10757.

93 Q. Gong, Y. Wang, Q. Hu, J. Zhou, R. Feng, P. N. Duchesne, P. Zhang, F. Chen, N. Han and Y. Li, Ultrasmall and phase-pure W_2C nanoparticles for efficient electrocatalytic and photoelectrochemical hydrogen evolution, *Nat. Commun.*, 2016, **7**, 1–8.

94 Y. Zhou, J. Xu, C. Lian, L. Ge, L. Zhang, L. Li, Y. Li, M. Wang, H. Liu and Y. Li, Carbon impurity-free, novel Mn, N co-doped porous Mo_2C nanorods for an efficient and stable hydrogen evolution reaction, *Inorg. Chem. Front.*, 2019, **6**, 2464–2471.

95 W. Xiao, L. Zhang, D. Bukhvalov, Z. Chen, Z. Zou, L. Shang, X. Yang, D. Yan, F. Han and T. Zhang, Hierarchical ultrathin carbon encapsulating transition metal doped MoP electrocatalysts for efficient and pH-universal hydrogen evolution reaction, *Nano Energy*, 2020, 104445.

96 C. Tang, R. Zhang, W. Lu, Z. Wang, D. Liu, S. Hao, G. Du, A. M. Asiri and X. Sun, Energy-saving electrolytic hydrogen generation: Ni_2P nanoarray as a high-performance non-noble-metal Electrocatalyst, *Angew. Chem., Int. Ed.*, 2017, **56**, 842–846.

97 X. Yang, A.-Y. Lu, Y. Zhu, M. N. Hedhili, S. Min, K.-W. Huang, Y. Han and L.-J. Li, CoP nanosheet assembly grown on carbon cloth: A highly efficient electrocatalyst for hydrogen generation, *Nano Energy*, 2015, **15**, 634–641.

98 H. Jin, X. Liu, Y. Jiao, A. Vasileff, Y. Zheng and S.-Z. Qiao, Constructing tunable dual active sites on two-dimensional C_3N_4@ MoN hybrid for electrocatalytic hydrogen evolution, *Nano Energy*, 2018, **53**, 690–697.

99 Q. Liu, L. Xie, F. Qu, Z. Liu, G. Du, A. M. Asiri and X. Sun, A porous Ni_3N nanosheet array as a high-performance non-noble-metal catalyst for urea-assisted electrochemical hydrogen production, *Inorg. Chem. Front.*, 2017, **4**, 1120–1124.

100 H. Vrubel and X. Hu, Molybdenum boride and carbide catalyze hydrogen evolution in both acidic and basic solutions, *Angew. Chem., Int. Ed.*, 2012, **51**, 12703–12706.

101 P. R. Jothi, Y. Zhang, J. P. Scheifers, H. Park and B. P. T. Fokwa, Molybdenum diboride nanoparticles as a highly efficient electrocatalyst for the hydrogen evolution reaction, *Sustainable Energy Fuels*, 2017, **1**, 1928–1934.

102 H. Park, Y. Zhang, E. Lee, P. Shankhari and B. Fokwa, High-Current-Density HER Electrocatalysts: Graphene-like Boron Layer and Tungsten as Key Ingredients in Metal Diborides, *ChemSusChem*, 2019, **12**, 3726–3731.

103 G.-F. Wei, L.-R. Zhang and Z.-P. Liu, Group-VIII transition metal boride as promising hydrogen evolution reaction catalysts, *Phys. Chem. Chem. Phys.*, 2018, **20**, 27752–27757.

104 L. Chen, L.-R. Zhang, L.-Y. Yao, Y.-H. Fang, L. He, G.-F. Wei and Z.-P. Liu, Metal boride better than Pt: HCP Pd_2B as a superactive hydrogen evolution reaction catalyst, *Energy Environ. Sci.*, 2019, **12**, 3099–3105.

105 L. T. Alameda, C. F. Holder, J. L. Fenton and R. E. Schaak, Partial etching of Al from MoAlB single crystals to expose catalytically active basal planes for the hydrogen evolution reaction, *Chem. Mater.*, 2017, **29**, 8953–8957.

106 S. Dutta, H. Han, M. Je, H. Choi, J. Kwon, K. Park, A. Indra, K. M. Kim, U. Paik and T. Song, Chemical and structural engineering of transition metal boride towards excellent and sustainable hydrogen evolution reaction, *Nano Energy*, 2020, **67**, 104245.

107 Z. Zhuang, Y. Li, Z. Li, F. Lv, Z. Lang, K. Zhao, L. Zhou, L. Moskaleva, S. Guo and L. Mai, MoB/g-C_3N_4 interface materials as a schottky catalyst to boost hydrogen evolution, *Angew. Chem., Int. Ed.*, 2018, **57**, 496–500.

108 Z. W. Seh, J. Kibsgaard, C. F. Dickens, I. Chorkendorff, J. K. Nørskov and T. F. Jaramillo, Combining theory and experiment in electrocatalysis: Insights into materials design, *Science*, 2017, **355**, eaad4998.

109 N.-T. Suen, S.-F. Hung, Q. Quan, N. Zhang, Y.-J. Xu and H. M. Chen, Electrocatalysis for the oxygen evolution reaction: recent development and future perspectives, *Chem. Soc. Rev.*, 2017, **46**, 337–365.

110 O. Diaz-Morales, S. Raaijman, R. Kortlever, P. J. Kooyman, T. Wezendonk, J. Gascon, W. Fu and M. Koper, Iridium-based double perovskites for efficient water oxidation in acid media, *Nat. Commun.*, 2016, **7**, 1–6.

111 L. C. Seitz, C. F. Dickens, K. Nishio, Y. Hikita, J. Montoya, A. Doyle, C. Kirk, A. Vojvodic, H. Y. Hwang and J. K. Norskov, A highly active and stable IrOx/$SrIrO_3$ catalyst for the oxygen evolution reaction, *Science*, 2016, **353**, 1011–1014.

112 C. W. Song, H. Suh, J. Bak, H. B. Bae and S.-Y. Chung, Dissolution-induced surface roughening and oxygen evolution electrocatalysis of alkaline-earth iridates in acid, *Chem*, 2020, **6**, 314.

113 Y. Liu, X. Liang, L. Gu, Y. Zhang, G.-D. Li, X. Zou and J.-S. Chen, Corrosion engineering towards efficient oxygen evolution electrodes with stable catalytic activity for over 6000 hours, *Nat. Commun.*, 2018, **9**, 1–10.

114 L. Lv, Z. Yang, K. Chen, C. Wang and Y. Xiong, 2D layered double hydroxides for oxygen evolution reaction: from fundamental design to application, *Adv. Energy Mater.*, 2019, **9**, 1803358.

115 J. Zhang, J. Liu, L. Xi, Y. Yu, N. Chen, S. Sun, W. Wang, K. M. Lange and B. Zhang, Single-atom Au/NiFe layered double hydroxide electrocatalyst: probing the origin of

activity for oxygen evolution reaction, *J. Am. Chem. Soc.*, 2018, **140**, 3876–3879.

116 J. Suntivich, K. J. May, H. A. Gasteiger, J. B. Goodenough and Y. Shao-Horn, A perovskite oxide optimized for oxygen evolution catalysis from molecular orbital principles, *Science*, 2011, **334**, 1383–1385.

117 A. Grimaud, K. J. May, C. E. Carlton, Y.-L. Lee, M. Risch, W. T. Hong, J. Zhou and Y. Shao-Horn, Double perovskites as a family of highly active catalysts for oxygen evolution in alkaline solution, *Nat. Commun.*, 2013, **4**, 2439.

118 X. Li, H. Wang, Z. Cui, Y. Li, S. Xin, J. Zhou, Y. Long, C. Jin and J. B. Goodenough, Exceptional oxygen evolution reactivities on $CaCoO_3$ and $SrCoO_3$, *Sci. Adv.*, 2019, **5**, eaav6262.

119 H. Wang, J. Wang, Y. Pi, Q. Shao, Y. Tan and X. Huang, Double Perovskite $LaFe_xNi_{1-x}O_3$ nanorods enable efficient oxygen evolution electrocatalysis, *Angew. Chem., Int. Ed.*, 2019, **58**, 2316–2320.

120 L. Li, Y. Zhang, J. Li, W. Huo, B. Li, J. Bai, Y. Cheng, H. Tang and X. Li, Facile synthesis of yolk-shell structured $ZnFe_2O_4$ microspheres for enhanced electrocatalytic oxygen evolution reaction, *Inorg. Chem. Front.*, 2019, **6**, 511–520.

121 Y. Tong, H. Mao, Y. Xu and J. Liu, Oxygen vacancies confined in Co_3O_4 quantum dots for promoting oxygen evolution electrocatalysis, *Inorg. Chem. Front.*, 2019, **6**, 2055–2060.

122 J. Li, D. Chu, H. Dong, D. R. Baker and R. Jiang, Boosted oxygen evolution reactivity by igniting double exchange interaction in spinel oxides, *J. Am. Chem. Soc.*, 2020, **142**, 50–54.

123 B. Zhang, X. Zheng, O. Voznyy, R. Comin, M. Bajdich, M. García-Melchor, L. Han, J. Xu, M. Liu and L. Zheng, Homogeneously dispersed multimetal oxygen-evolving catalysts, *Science*, 2016, **352**, 333–337.

124 R. D. Smith, M. S. Prévot, R. D. Fagan, Z. Zhang, P. A. Sedach, M. K. J. Siu, S. Trudel and C. P. Berlinguette, Photochemical route for accessing amorphous metal oxide materials for water oxidation catalysis, *Science*, 2013, **340**, 60–63.

125 T. Ling, T. Zhang, B. Ge, L. Han, L. Zheng, F. Lin, Z. Xu, W. B. Hu, X. W. Du and K. Davey, Well-dispersed nickel- and zinc-tailored electronic structure of a transition metal oxide for highly active alkaline hydrogen evolution reaction, *Adv. Mater.*, 2019, **31**, 1807771.

126 K. Xu, P. Chen, X. Li, Y. Tong, H. Ding, X. Wu, W. Chu, Z. Peng, C. Wu and Y. Xie, Metallic nickel nitride nanosheets realizing enhanced electrochemical water oxidation, *J. Am. Chem. Soc.*, 2015, **137**, 4119–4125.

127 L.-A. Stern, L. Feng, F. Song and X. Hu, Ni_2P as a Janus catalyst for water splitting: the oxygen evolution activity of Ni_2P nanoparticles, *Energy Environ. Sci.*, 2015, **8**, 2347–2351.

128 X. Zou, Y. Wu, Y. Liu, D. Liu, W. Li, L. Gu, H. Liu, P. Wang, L. Sun and Y. Zhang, In situ generation of bifunctional, efficient Fe-based catalysts from mackinawite iron sulfide for water splitting, *Chem*, 2018, **4**, 1139–1152.

129 P. W. Menezes, C. Walter, J. N. Hausmann, R. Beltrán-Suito, C. Schlesiger, S. Praetz, V. Yu. Verchenko, A. V. Shevelkov and M. Driess, Boosting water oxidation through in situ electroconversion of manganese gallide: an intermetallic precursor approach, *Angew. Chem., Int. Ed.*, 2019, **58**, 16569–16574.

130 X. Ma, J. Wen, S. Zhang, H. Yuan, K. Li, F. Yan, X. Zhang and Y. Chen, Crystal Co_xB (x = 1–3) synthesized by a ball-milling method as high-performance electrocatalysts for the oxygen evolution reaction, *ACS Sustainable Chem. Eng.*, 2017, **5**, 10266–10274.

131 A.-M. Zieschang, J. D. Bocarsly, J. Schuch, C. V. Reichel, B. Kaiser, W. Jaegermann, R. Seshadri and B. Albert, Magnetic and electrocatalytic properties of nanoscale cobalt boride, Co_3B, *Inorg. Chem.*, 2019, **58**, 16609–16617.

132 H. Li, P. Wen, Q. Li, C. Dun, J. Xing, C. Lu, S. Adhikari, L. Jiang, D. L. Carroll and S. M. Geyer, Earth-abundant iron diboride (FeB_2) nanoparticles as highly active bifunctional electrocatalysts for overall water splitting, *Adv. Energy Mater.*, 2017, **7**, 1700513.

133 W. J. Jiang, S. Niu, T. Tang, Q. H. Zhang, X. Z. Liu, Y. Zhang, Y. Y. Chen, J. H. Li, L. Gu and L. J. Wan, Crystallinity-modulated electrocatalytic activity of a nickel (II) borate thin layer on Ni_3B for efficient water oxidation, *Angew. Chem., Int. Ed.*, 2017, **56**, 6572–6577.

134 H. Yuan, S. Wang, X. Gu, B. Tang, J. Li and X. Wang, One-step solid-phase boronation to fabricate self-supported porous FeNiB/FeNi foam for efficient electrocatalytic oxygen evolution and overall water splitting, *J. Mater. Chem. A*, 2019, **7**, 19554–19564.

135 D. K. Mann, J. Xu, N. E. Mordvinova, V. Yannello, Y. Ziouani, N. González-Ballesteros, J. P. Sousa, O. I. Lebedev, Y. V. Kolen'ko and M. Shatruk, Electrocatalytic water oxidation over $AlFe_2B_2$, *Chem. Sci.*, 2019, **10**, 2796–2804.

136 P. De Luna, C. Hahn, D. Higgins, S. A. Jaffer, T. F. Jaramillo and E. Sargent, What would it take for renewably powered electrosynthesis to displace petrochemical processes?, *Science*, 2019, **364**, eaav3506.

137 G. Qin, Q. Cui, A. Du, W. Wang and Q. Sun, Transition metal diborides: A new type of high-performance electrocatalysts for nitrogen reduction, *ChemCatChem*, 2019, **11**, 2624–2633.

138 Q. Li, C. Liu, S. Qiu, F. Zhou, L. He, X. Zhang and C. Sun, Exploration of iron borides as electrochemical catalysts for the nitrogen reduction reaction, *J. Mater. Chem. A*, 2019, **7**, 21507–21513.

139 B. Zhang, L. Fan, J. Hu, J. Gu, B. Wang and Q. Zhang, MnB_2 nanosheet and nanotube: stability, electronic structures, novel functionalization and application for Li-ion batteries, *Nanoscale*, 2019, **11**, 7857–7865.

140 Y. Chen, T. Zhou, L. Li, W. K. Pang, X. He, Y.-N. Liu and Z. Guo, Interfacial engineering of nickel boride/metaborate and its effect on high energy density asymmetric supercapacitors, *ACS Nano*, 2019, **13**, 9376–9385.

141 X. Lu, J. Xie, S.-Y. Liu, A. Adamski, X. Chen and X. Li, Low-cost $Ni_3B/Ni(OH)_2$ as an ecofriendly hybrid cocatalyst for remarkably boosting photocatalytic H_2 production over g-C_3N_4 nanosheets, *ACS Sustainable Chem. Eng.*, 2018, 13140–13150.

142 H. Yuan, Z. Li and J. Yang, Transition-metal diboride: a new family of two-dimensional materials designed for selective CO_2 electroreduction, *J. Phys. Chem. C*, 2019, **123**, 16294–16299.

143 N. Patel, R. Fernandes, G. Guella, A. Kale, A. Miotello, B. Patton and C. Zanchetta, Structured and nanoparticle assembled Co-B thin films prepared by pulsed laser deposition: A very efficient catalyst for hydrogen production, *J. Phys. Chem. C*, 2008, **112**, 6968–6976.